

## Exactly central heavy-ion collisions by nuclear hydrodynamics

Henry H. K. Tang\*

*A. W. Wright Nuclear Structure Laboratory, Yale University, New Haven, Connecticut 06520*

Cheuk-Yin Wong

*Physics Division, Oak Ridge National Laboratory, Oak Ridge, Tennessee 37830*

(Received 17 September 1979)

We study the dynamics of heavy-ion collisions using the hydrodynamical description and focus our attention on the head-on collisions which provide the most favorable case for such a description. Angular distributions and energy distributions were obtained for various combinations of projectiles and targets of equal and unequal masses in the energy range from 50 to 400 MeV per projectile nucleon. It is found that regions of high density (the shock regions) are formed during the collisions and that the angular and energy distributions for many of these collisions have prominent features. In the collision of a small projectile with a heavy target, there is the forward angular peak of slow dissociated particles which represent much of the projectile nuclear matter stopped in the larger target nucleus, in addition to the nucleons from the expansions of the shock region. There is the side angular peak corresponding to the sidesplash of the target nuclear matter due to the impact of the projectile. There is also the backward angular peak due to the expansion of the shock region into the backward direction. In the collision of two equal nuclei, there are only the forward angular peak and the side angular peak. The effects of viscosity and thermal conductivity are investigated and found to affect the angular and energy distributions of the reaction products.

[ NUCLEAR REACTIONS Heavy-ion reactions, nuclear hydrodynamics,  $^{20}\text{Ne}$   
 $+^{197}\text{Au}$  and  $^{208}\text{Pb}+^{208}\text{Pb}$  at 50, 100, 250, and 400 MeV per projectile nucleon.  
 Nuclear viscosity and thermal conductivity. ]

### I. INTRODUCTION

Our recent interest in high-energy, heavy-ion reactions stems in part from the possibility of probing the equation of state of nuclear matter, both with regard to its behavior at zero temperature and at high temperatures. Many exotic phenomena such as the pion condensation and density isomers manifest themselves in peculiar shapes of the equation of state.<sup>1</sup> As the equation of state enters prominently in the hydrodynamical description of the reaction process, it is desirable to ascertain to what degree the heavy-ion collision process can be described by hydrodynamics. Although much discussion and investigation has been made on the theoretical foundation of nuclear hydrodynamics,<sup>2-6</sup> in the final analysis, it is a direct confrontation of the results of hydrodynamical calculations with experiments which will validate or negate the hydrodynamical description. The recent observations by Gutbrod and collaborators<sup>7</sup> that many features of the heavy-ion collisions at intermediate energies may have hydrodynamical origin gives additional impetus to the treatment of heavy-ion collision in terms of nuclear hydrodynamics.

The advantages of a hydrodynamical treatment of the reaction process, if successful, are manifold. As different energy heavy ions lead to

different compressed densities, the equation of state can, in principle, be traced by using projectiles of different energies. Furthermore, one may also obtain the transport coefficients of nuclear matter which otherwise cannot be obtained by other means. For these reasons, one may wish to push the hydrodynamical description as far as possible and see how it could perhaps describe some aspects of heavy-ion collisions.

It is clear from the outset that not all the nuclear collisions can be described properly by nuclear hydrodynamics. For example, peripheral and transfer reactions are unlikely to be described well by nuclear hydrodynamics as the interaction time involved is short compared with the time necessary to bring the system into local equilibrium. It is necessary to be selective in choosing the proper case for treatment. The interaction time increases as the impact parameter decreases. Head-on collisions involving large nuclei present favorable cases where nuclear hydrodynamics may perhaps be a valid description. For this reason, we focus our attention on head-on collisions, with the hope of exploring only the region around  $l=0$  at a later time.

Past treatments of numerical nuclear hydrodynamics<sup>5,6,8</sup> centered on the comparison of theoretical results with the experimental single-particle inclusive data.<sup>9</sup> The objective is to ob-

tain the angular distribution after a summation over all the impact parameters. Earlier work deals with the case of head-on collisions.<sup>10</sup> The numerical technique used is the PIC (particle-in-cell) method. As no long-range interaction is used, the nuclear surface is given as a sharp surface which introduces the problem of negative pressure. Furthermore, viscosity and thermal conductivity are not taken into account. Another treatment of the hydrodynamical problem made use of the assumption of irrotational flow<sup>11</sup> and a qualitative representation of the mach cone concept.<sup>12</sup> Conjectures based on the latter are, however, not substantiated by the detailed calculations of Amsden *et al.*<sup>10</sup> Still another treatment by Wong, Tang, and collaborators<sup>13-17</sup> discussed shock waves in supersonic heavy-ion collisions and later introduced the long-range interaction to describe the nuclear surface. The numerical method is based on the FCT (flux-corrected-transport) method of Boris and Book<sup>18</sup> which allows simple incorporation of viscosity and thermal conductivity. One-dimensional hydrodynamical calculations based on such a model have been reported previously.<sup>14</sup> Two-dimensional calculations for the collision of one infinite cylinder of nuclear matter with another were also performed and will be reported elsewhere.<sup>16</sup> This paper deals with three-dimensional head-on collisions. A preliminary report, based on the work of Wong, Welton, and Maruhn, was presented previously.<sup>17</sup>

This paper is organized as follows. In Sec. II the basic equations of nuclear hydrodynamics are presented. A brief description of the genealogy of nuclear hydrodynamics and its connection with the many-body theory is given. A criterion of its validity in terms of the thermal relaxation time is also discussed. In Sec. III an estimate of the nuclear transport coefficients is made. The shear viscosity and the thermal conductivity are estimated from the Landau-Fermi liquid theory and the compressional viscosity from the width of the giant monopole resonance. In Sec. IV we discuss our choice of the equation of state and other parameters for the nuclear fluid. Section V presents a detailed description and discussion of the results. They are the calculations for head-on collisions of  $^{20}\text{Ne} + ^{197}\text{Au}$  and  $^{208}\text{Pb} + ^{208}\text{Pb}$  at the bombarding energies of 50, 100, 250, and 400 MeV per projectile nucleon, both with and without viscosity and thermal conductivity. Special features of the hydrodynamical description and the significance of dissipation in the dynamics are emphasized in order to facilitate future confrontations with experiments. Finally, Sec. VI summarizes the main results and remarks

on future investigations along this line. An appendix is attached in which some technical aspects of the numerical problem are discussed.

A very important parameter in the present discussion is the initial kinetic energy of the colliding nuclei. For simplicity, we shall adopt the convention of measuring the energy in terms of the kinetic energy of the projectile per projectile nucleon while the target is at rest. Furthermore, in the collision of unequal nuclei we shall take the lighter nucleus as the projectile. The energy parameter is then expressed as  $E_{1ab}/A_p$ , where  $E_{1ab}$  is the laboratory kinetic energy of the projectile and  $A_p$  is the projectile mass. For simplicity, this quantity is sometimes expressed as simply as  $E/A$ .

## II. BASIC EQUATIONS OF NUCLEAR HYDRODYNAMICS

The connection between nuclear hydrodynamics and a more fundamental quantum many-body theory has been extensively studied by various workers.<sup>1-6,19-21</sup> We shall briefly discuss the results of Refs. 20 and 21 with regard to the connection between nuclear hydrodynamics and the many-body theory. This connection can be depicted in Fig. 1. One can start with the exact many-body theory and obtain the extended time-dependent Hartree-Fock (ETDHF) approximation.<sup>20</sup> In this approximation, both the effect of the mean-field and particle collisions are considered. Next, one goes to a classical transcription<sup>21</sup> by interpreting the Wigner function in the ETDHF approximation as the classical distribution function. The resultant approximate Vlasov-Boltzmann equation forms the basis from which much statistical dynamics can be extracted. One can introduce the quantity of local entropy field and prove with the Vlasov-Boltzmann equation that the total time derivative of the local entropy never decreases. It is natural to speak of the situation when the local entropy is stationary as the state of local (thermal) equilibrium. One can prove<sup>21</sup> further that when local equilibrium is attained, the local momentum distribution is characterized by a Fermi-Dirac distribution. The parameters in the distribution are (1) the local temperature, (2) the local Fermi energy which is related to the local density, and (3) the displacement of the Fermi-Dirac spherical distribution from the origin which is related to the local velocity field. Thus, when there is local equilibrium, the local stress tensor, as obtained from the momentum distribution, depends only on the local temperature, the local density, and the local velocity field. Then, by using the well-known Enskog-Chapman procedure, one can ap-

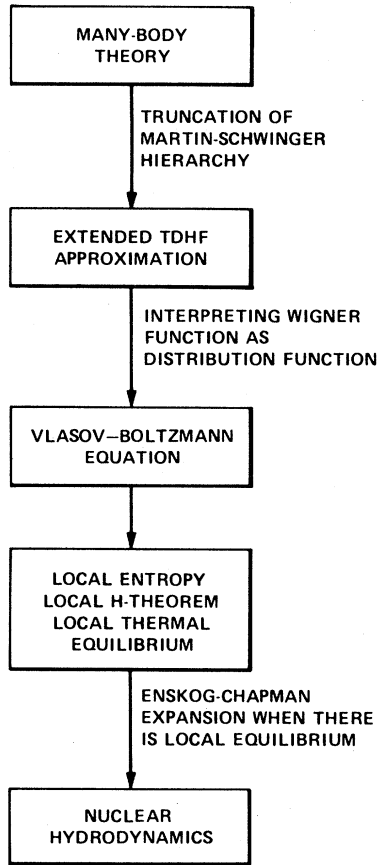


FIG. 1. Genealogy of nuclear hydrodynamics and its connection with the many-body theory.

proximate the Vlasov-Boltzmann equation by those of hydrodynamics,<sup>22</sup> namely the continuity equation

$$\frac{\partial n}{\partial t} + \nabla \cdot (n\vec{u}) = 0, \quad (2.1)$$

the Navier-Stokes equations

$$\frac{\partial(mu_i)}{\partial t} + \sum_{j=1}^3 \nabla_j \left[ nu_j u_i + \frac{1}{m} (p\delta_{ij} + p'_{ij}) \right] = -\frac{n}{m} \nabla_i \int d^3r' n(\vec{r}', t) V_L(\vec{r}, \vec{r}'), \quad (2.2)$$

and the thermal energy density equation

$$\frac{\partial(nE_T)}{\partial t} + \nabla \cdot (nE_T \vec{u}) = -p_T \nabla \cdot \vec{u} + \nabla \cdot (\kappa \nabla T) - \sum_{ij} p'_{ij} \frac{\partial u_i}{\partial x_j}. \quad (2.3)$$

Here, in the hydrodynamical picture, the basic dynamical variables are the number density field  $n$ , the velocity field  $\vec{u}$ , and the thermal energy field  $E_T$ . The continuity equation (2.1) describes

the time evolution of the density field. The Navier-Stokes equations (2.2) are equations for the current density. In Eq. (2.2),  $m$  is the nucleonic mass and  $p$  is the total pressure which can be obtained from the equation of state of the nuclear fluid. The dissipative behavior of the system is accounted for by the viscosity stress tensor  $p'_{ij}$  which is defined as

$$p'_{ij} \equiv - \left\{ \eta \left[ \left( \frac{\partial u_i}{\partial x_j} + \frac{\partial u_j}{\partial x_i} \right) - \frac{2}{3} \delta_{ij} \nabla \cdot \vec{u} \right] + \delta_{ij} \zeta \nabla \cdot \vec{u} \right\}, \quad (2.4)$$

where  $\eta$  and  $\zeta$  are the transport coefficients of shear and compressional viscosity, respectively. The force-density term on the right hand side of Eq. (2.2) is due to the long-range part of the nucleon-nucleon interaction. In the thermal energy density equation (2.3),  $p_T$  is the thermal pressure which can be related to the equation of state,  $\kappa$  is the coefficient of thermal conductivity, and  $T$ , the temperature field of the nuclear fluid. The choice of the transport coefficients  $\eta$ ,  $\zeta$ , and  $\kappa$ , the parametrizations of the equation of state and the auxiliary quantities  $p$ ,  $p_T$ , and  $T$  will be subjects of discussion in the later sections.

As the establishment of local equilibrium is necessary for the reduction of the Vlasov-Boltzmann equation to nuclear hydrodynamics, the crucial question becomes whether the relaxation time leading to local equilibrium is short compared with the total time involved in the interaction. The magnitude of this relaxation time is yet to be firmly established, although attempts are being made to calculate it for some model cases.<sup>23-25</sup> We can, however, make a rough estimate of the magnitude. Previously, in connection with the ETDHF approximation,<sup>20</sup> we argued from the magnitude of the level densities and of the two-body matrix elements that (global) thermal equilibrium for a slightly excited nucleus of mass number  $A$  could be established within a time of

$$\tau_{\text{relaxation}} \approx \frac{4000}{A} \text{fm}/c. \quad (2.5)$$

Indeed, recent experimental studies<sup>26</sup> of the spectrum of evaporated neutrons from the deep-inelastic collision fragments indicate that the relaxation time for thermal equilibrium of the composite system is approximately  $10^{-22}$  sec ( $\sim 30$  fm/c). The estimate of Eq. (2.5) agrees with these experimental results. A model calculation<sup>23</sup> of the approach to equilibrium of an irregular momentum distribution leading to a temperature of 8.5 MeV also gives a relaxation time of 40 fm/c.

In heavy-ion collisions, the momentum distribution of the nucleons in the colliding region is approximately a Fermi bisphere whose centers are separated by the relative momentum determined by the kinetic energy per projectile nucleon. As the blocking due to the Pauli principle becomes less inhibitive when the separation of the centers in the Fermi bi-sphere increases, the fraction of nucleons capable of making a two-body collision and the phase space of the final states increase with bombarding energy. One expects that the relaxation time decreases with increasing bombarding energy until the energy is so high that the bisphere separates into two disjointed Fermi spheres. Thereafter, the relaxation time becomes less sensitive to the change of bombarding energy.<sup>24</sup> Thus, for the bombardment energy in the range of 250 MeV per nucleon to 2.1 GeV per nucleon (where the Fermi bi-sphere becomes disjointed) the relaxation time was found to be of the order of 5 fm/c.<sup>24</sup> This result agrees with the estimate of Bertsch<sup>25</sup> based on the moment of the collision integral for low-energy heavy-ion collisions

$$\tau \sim \frac{1000 \text{ MeV fm/c}}{(E_{1ab}/A_p)}, \quad (2.6)$$

where  $A_p$  is the projectile mass number. The relaxation time in the intermediate energy range is therefore roughly 50 fm/c for an energy of  $E_{1ab}/A_p = 20$  MeV per nucleon and 4 fm/c for  $E_{1ab}/A_p = 250$  MeV per nucleon.

Hydrodynamical description will be a proper approximation if the interaction time for the reaction process is large compared with the thermal relaxation time. The interaction time for a head-on collision of  $^{20}\text{Ne}$  on  $^{197}\text{Au}$  is about 200 fm/c for a collision with an energy of  $E_{1ab}/A_p = 50$  MeV per nucleon, 130 fm/c for a collision with an energy of  $E_{1ab}/A_p = 100$  MeV per nucleon, and 100 fm/c for a collision with energy of  $E_{1ab}/A_p = 250$  MeV per nucleon. Therefore, it appears that at least for these collisions involving large nuclei, the hydrodynamical description may be appropriate. Of course, one is reminded that these estimates of relaxation time are based on a nuclear matter equilibration. There are effects due to finite sizes, nuclear surface, and shell structure which may affect these estimates. In the final analysis, a direct confrontation between experimental and theoretical results is needed to establish or reject nuclear hydrodynamics for some aspects of heavy-ion collisions.

### III. TRANSPORT COEFFICIENTS

Not much is known about the transport coefficients of the nuclear fluid. At the present, they can only be estimated from the theories. Direct comparison of the predictions by assuming different sets of transport coefficients and confrontation with experimental results will eventually allow one to determine these transport coefficients.

We shall estimate the shear viscosity and thermal conductivity from the Vlasov-Boltzmann equation which is embodied in the Landau-Fermi liquid theory. We shall estimate the compressional viscosity from the width of the giant monopole resonance. Using the Born approximation and a procedure developed by Baym and Pethick<sup>27</sup> which was suggested earlier by Sykes and Brooker,<sup>28</sup> we obtain the thermal conductivity as

$$\frac{\kappa}{k_B} = \frac{1}{3\pi} \frac{p_f^3}{m^2 k_B T} \langle d\sigma/d\Omega \rangle \times \sum_{\nu=2,4,6,\dots} \frac{(2\nu+1)}{\nu(\nu+1)[\nu(\nu+1)-2\lambda_\kappa]} \quad (3.1)$$

where

$$\langle \frac{d\sigma}{d\Omega} \rangle = \int \frac{d\Omega(\theta, \phi)}{4\pi} \left\{ g \frac{d\sigma}{d\Omega}(\Theta_{13}(\theta, \phi)) \right\} / 2 \cos \frac{\theta}{2} \quad (3.2)$$

and

$$\lambda_\kappa \langle \frac{d\sigma}{d\Omega} \rangle = \int \frac{d\Omega(\theta, \phi)}{4\pi} \left\{ g \frac{d\sigma}{d\Omega}[\Theta_{13}(\theta, \phi)] \right\} \times (1 + 2 \cos \theta) / 2 \cos \frac{\theta}{2}. \quad (3.3)$$

In the above expressions,  $\theta$  is the angle between  $\vec{p}_1$  and  $\vec{p}_2$ , while  $\phi$  is the dihedral angle between the planes  $\vec{p}_1 \times \vec{p}_2$  and  $\vec{p}_3 \times \vec{p}_4$ ,  $\Theta_{13}$  is the angle between  $\vec{p}_1$  and  $\vec{p}_3$ , and  $g$  is the degeneracy of the nuclear fluid which is 4 in this case. Upon taking a constant value of 1.0 fm<sup>2</sup>/sr from  $(p, p)$  scattering<sup>29</sup> at a relative kinetic energy of  $\epsilon_f \sim 40$  MeV for  $d\sigma/d\Omega$ , we obtain

$$\frac{\kappa}{k_B} = \frac{0.4224 \text{ MeV c/fm}^2}{k_B T}, \quad (3.4)$$

where  $k_B T$  is given in MeV. One can follow the same procedure of Baym and Pethick<sup>27</sup> to obtain the shear viscosity coefficient

$$\eta = \frac{1}{15\pi^3} \frac{p_f^5}{m^2 (k_B T)^2} \frac{1}{\langle d\sigma/d\Omega \rangle} \times \sum_{\nu=1,3,5,\dots} \frac{2\nu+1}{\nu(\nu+1)[\nu(\nu+1)-2\lambda_\eta]}, \quad (3.5)$$

where  $\langle d\sigma/d\Omega \rangle$  is as given before and

$$\lambda_\eta \langle \frac{d\sigma}{d\Omega} \rangle = \int \frac{d\Omega(\theta, \phi)}{4\pi} \left\{ g \frac{d\sigma}{d\Omega}[\Theta_{13}(\theta, \phi)] \right\} \left( -1 + 3 \sin^4 \frac{\theta}{2} \sin^2 \phi \right) / 2 \cos \frac{\theta}{2}. \quad (3.6)$$

Again, upon using a constant value of  $1.0 \text{ fm}^2/\text{sr}$  for  $d\sigma/d\Omega$ , we obtain

$$\eta = \frac{675.39 \text{ (MeV)}^3}{(k_B T)^2 \text{ fm}^2 \cdot c}. \quad (3.7)$$

The transport coefficients are therefore sensitive functions of the local temperature. It is known, however, that the temperature reached in the collision of heavy ions with a few hundred MeV per nucleon is about 30 MeV.<sup>30</sup> So, for our first estimate of an average transport coefficient, we use 30 MeV as the temperature parameter to obtain

$$\kappa = 0.014 \text{ c/fm}^2, \quad (3.8)$$

and

$$\eta = 0.75 \text{ MeV}/(\text{fm}^3 \text{ c}). \quad (3.9)$$

To estimate the compressional viscosity coefficient from the width of the giant monopole resonance, we consider the equation of motion for small amplitude oscillations

$$\frac{\partial n}{\partial t} + \nabla \cdot (n\vec{u}) = 0 \quad (3.10)$$

and

$$\frac{\partial}{\partial t} n\vec{u} + 0(\vec{n}^2) = -a^2 \nabla n + (\xi - \frac{2}{3}\eta) \nabla(\nabla \cdot \vec{u}), \quad (3.11)$$

where  $a$  is the speed of sound related to the incompressibility  $K$  by

$$a = (K/9m)^{1/2}. \quad (3.12)$$

From this set of equations, the monopole oscillation frequency becomes complex and is given by

$$\omega = \omega_0 \left( 1 - \frac{i(\xi - \frac{2}{3}\eta)\pi^2 R^2}{2mn_0\omega_0 R^2} \right), \quad (3.13)$$

where  $\hbar\omega_0 = (\hbar\pi/R)(K/9m)^{1/2}$  is the eigenenergy of the monopole oscillation in the absence of compressional viscosity,  $R$  is the radius of the nucleus, and  $n_0$  the normal density of nuclear matter. Identifying the imaginary part of the frequency with the width  $\Gamma$  of the giant monopole resonance, we have

$$\Gamma = \hbar \frac{(\xi - \frac{2}{3}\eta)\pi^2 R^2}{2mn_0}. \quad (3.14)$$

For  $^{208}\text{Pb}$  the width of the giant monopole resonance is 2.5 MeV.<sup>31</sup> Thus, the compressional coefficient is

$$\xi = 18.76 \text{ MeV}/(\text{fm}^2 \text{ c}). \quad (3.15)$$

#### IV. EQUATION OF STATE AND OTHER PARAMETERS

##### A. Energy density of the nuclear fluid

The use of an equation of state is a characteristic of nuclear hydrodynamics. In the present investigation, the internal energy per nucleon of the nuclear fluid assumes a mathematically simple, but physically plausible, form

$$E_{in}(n, \sigma) = E_0(n) + E_T(n, \sigma), \quad (4.1)$$

where  $E_0$  is the zero-temperature part of the internal energy per nucleon, depending only on the local density field, and  $E_T$  the thermal part which depends on the local density field as well as the specific entropy  $\sigma$  (or temperature  $T$ ). The zero-temperature part is taken to be of the form<sup>32</sup>

$$E_0(n) = b_0 n^{2/3} + b_1 n^{3/3} + b_2 n^{4/3} + b_3 n^{5/3} \quad (4.2)$$

and the thermal part is parametrized by the Fermi gas model

$$E_T(n, \sigma) = \frac{1}{2} \frac{\hbar^2}{m} \left( \frac{6}{4\pi} \right)^{2/3} \sigma^2 n^{2/3}, \quad (4.3)$$

which can also be re-expressed in terms of the temperature as

$$E_T(n, \sigma) = \frac{1}{2} \frac{m}{\hbar^2} \left( \frac{4\pi}{6} \right)^{2/3} n^{-2/3} T^2, \quad (4.4)$$

With this form of the internal energy function, the coefficients  $b_i$ 's in Eq. (4.2) can be uniquely determined as follows. The leading coefficient  $b_0$  is taken to be the same as the corresponding one in the Fermi gas model

$$b_0 = 75.01 \text{ MeV fm}^2. \quad (4.5)$$

The other coefficients can then be determined by three known bulk properties of nuclei. They are the normal density at equilibrium

$$n_0 = 0.17 \text{ fm}^{-3}, \quad (4.6)$$

the binding energy per particle

$$E_B = -16.5 \text{ MeV} \quad (4.7)$$

and the coefficient of nuclear incompressibility at equilibrium density [estimated from giant monopole resonance of  $^{208}\text{Pb}$  (Ref. 33)]

$$K(n_0) = 186 \text{ MeV}. \quad (4.8)$$

With the equation of state given, the pressure terms can now be obtained from standard thermodynamic relations. The total pressure of the nuclear fluid is of the form

$$p(n, \sigma) = p_0(n) + p_T(n, \sigma), \quad (4.9)$$

where the zero-temperature part is now given by

$$p_0 = n^{5/3} \left( \frac{2}{3} b_0 + b_1 n^{1/3} + \frac{4}{3} b_2 n^{2/3} + \frac{5}{3} b_3 n^{3/3} \right)$$

and the thermal part is given by

$$p_T = \frac{2}{3} n E_T. \quad (4.10)$$

### B. Interaction parameters

For the effective nucleon-nucleon interaction we adopt a parametrization similar to that used in microscopic theories such as the time-dependent Hartree-Fock theory.<sup>14</sup> This interaction is taken to contain a short-range part  $V_S$  and a long-range part  $V_L$ . The short-range component can be characterized by a delta function with density dependence. This, however, can be incorporated into the internal energy, while the long-range component can be taken to be the sum of a Yukawa interaction and the Coulomb interaction. The Yukawa interaction is

$$V_Y(\vec{r}, \vec{r}') = \beta \frac{e^{-\alpha|\vec{r}-\vec{r}'|}}{|\vec{r}-\vec{r}'|}, \quad (4.11)$$

with

$$\beta = -85 \text{ MeV fm} \quad (4.12)$$

and

$$\alpha = 1.5 \text{ fm}^{-1}. \quad (4.13)$$

These parameters,  $\beta$  and  $\alpha$ , are chosen to fit the binding energies and root-mean-squared radii of nuclei along the  $\beta$ -stability line. The Coulomb interaction is given as

$$V_c(\vec{r}, \vec{r}') = \left( \frac{Z_P + Z_T}{A_P + A_T} \right)^2 \frac{e^2}{|\vec{r} - \vec{r}'|}, \quad (4.14)$$

where  $(Z_P, A_P)$  and  $(Z_T, A_T)$  are the atomic and mass numbers of the projectile and target nuclei, respectively, and  $e$  the charge of an electron.

## V. RESULTS OF CALCULATIONS AND DISCUSSIONS

We shall discuss the specific features of several exactly central collisions which we have studied in the energy range from 50 MeV up to 400 MeV per nucleon. Here and henceforth, the bombarding energy is given in terms of the energy per projectile nucleon with the target at rest. Systematic studies of the other cases of non-head-on collisions will be reported elsewhere.<sup>16</sup> Our discussions will concentrate on the bombarding of  $^{20}\text{Ne}$  on  $^{197}\text{Au}$  targets and also that of  $^{208}\text{Pb}$  on  $^{208}\text{Pb}$  at various energies. In the subsequent discussion, we shall also refer to the case of equal projectile and target as the symmetric collision (or system) and the unequal projectile and target as asymmetric collision (or system).

To study the effects of dissipation on the dynamics, we shall compare calculations using two different sets of transport coefficients. They are

$$\eta, \zeta = 10^{-4} \text{ MeV/fm}^2 c$$

and (5.1)

$$\kappa = 10^{-4} c/\text{fm}^2,$$

which will be referred to as the "small" viscosity or simply the nonviscous or inviscid case in the text, and the values estimated in Sec. III

$$\eta = 0.75 \text{ MeV}/(\text{fm}^2 c),$$

$$\zeta = 18.76 \text{ MeV}/(\text{fm}^2 c), \quad (5.2)$$

and

$$\kappa = 0.014 c/\text{fm}^2,$$

which, for simplicity, will be referred to as the "large" viscosity or simply the viscous case in the text.

Each calculation is started with the nuclear surface of the projectile and target nuclei barely touching. The density distribution of each nucleus is obtained individually in a self-consistent manner as the distribution leading to static equilibrium. The nuclei are given velocity fields corresponding to the bombarding energy in question. With the initial conditions established, the complete set of hydrodynamical equations (2.1)–(2.3) is then solved for the subsequent times. Some numerical aspects of this problem will be discussed in the Appendix.

### A. $^{20}\text{Ne}$ on $^{197}\text{Au}$ at 250 MeV per nucleon

Figure 2 depicts the time evolution of the density field in the center-of-mass system for the collision for 250 MeV per projectile ( $^{20}\text{Ne}$ ) nucleon on  $^{197}\text{Au}$ . The plots shown are the cuts of density contours in the reaction plane, graded in levels of  $0.025 \text{ fm}^{-3}$ . To standardize our notations in subsequent discussions, we take the value  $0.15 \text{ fm}^{-3}$  to be the "normal nuclear density." The calculation shown in Fig. 2 is done with the small values of transport coefficients given in Eq. (5.1). At about  $10 \text{ fm}/c$ , a region of compressed nuclear matter is formed and has attained a density of about 1.5 times the normal value. The density continues rising in this region until a maximum value of  $0.35 \text{ fm}^{-3}$  is reached at about  $25 \text{ fm}/c$ . During the stage of compression, the density profile of this region has a very sharp jump as one goes from this region to the rest of the system or normal density. The thickness of the shock front is only slightly greater than the mesh size of  $0.6 \text{ fm}$ . The compressed region undergoes a forward displacement to the right as a whole as time proceeds. At about  $25 \text{ fm}/c$ , the Ne nucleus is entirely embedded in the target system and the maximum density of  $0.35 \text{ fm}^{-3}$  is also reached.

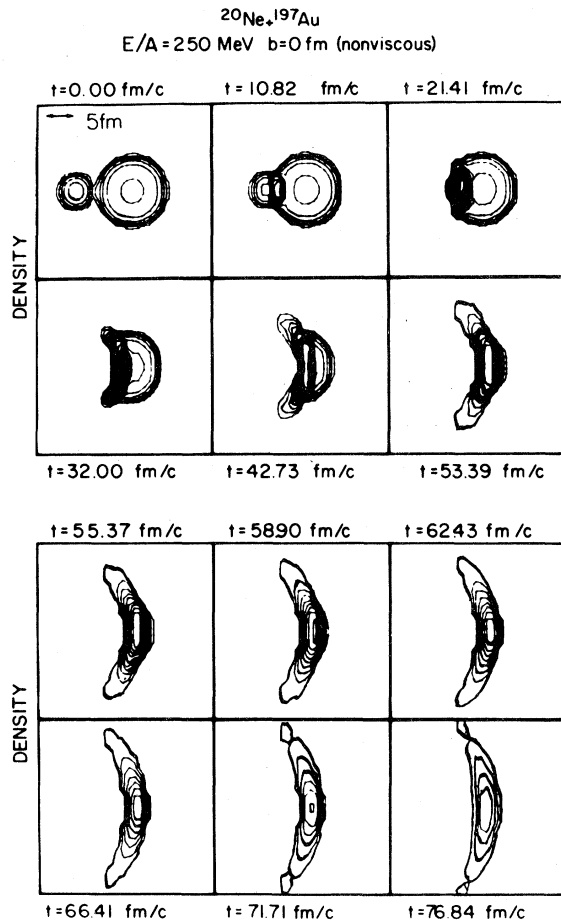


FIG. 2. Time evolution of the density field for  $^{20}\text{Ne} + ^{197}\text{Au}$  at 250 MeV per nucleon with small viscosity.

The compressed region maintains this maximum density for a few fm/c and then begins to relax. At 32 fm/c, due to the size of the target and the consequent time delay in transmitting the impulse of the collision, roughly half of the target system is still unperturbed. There are currents going into the compressed region directed from the target. However, this current encounters the forward propagation of the shock region and gives rise to an ejection of nuclear matter along a "side-wing" direction which is approximately  $120^\circ$  in the center-of-mass system. This side-wing expands outwards as the density in the compressed region drops from the maximum values. After 60 fm/c, the central density of the composite system drops back to the normal value and continues to decrease monotonically in time, while the volume of the system expands outwards irretrievably. This feature in the collision is similar to what was obtained previously.<sup>10</sup> To determine the angular and energy distributions,

we adopt the operational criteria that for such a case, the calculation is to be terminated once the maximum density drops to below 50% of the normal nuclear matter density. This is a reasonable operational criterion. For, when the maximum density drops below 50% of the normal matter density, the shortest separations between nucleons increase by 26% of the equilibrium separation. The average separation between nucleons increases even more than this value of 26% for the shortest separations. As nuclear interaction is a short-range interaction, the separation between nucleons in this dilute gas is probably too large for the nuclear interaction to become effective. The dilute gas can therefore be approximately described as a free fermion gas subject only to the Coulomb interaction. The final result of this reaction is interpreted as a complete dissociation into single particles. The knowledge of the density field and the velocity field at the end of the calculation allows us to compute both the angular and energy distributions of the outgoing nucleons. For our present calculations of angular and energy distributions, we even neglect the final state Coulomb interaction and the thermal velocities of the particles. They will probably shift and broaden the peaks in the angular and energy distributions slightly, but will not change the main features of the distributions. We hope to include these effects in the future.

Figure 3(a) shows the angular distribution  $dN/d\Omega$  in the center-of-mass system. The main structure has prominent forward and backward peaks which are, respectively, one and two orders of magnitude higher than the rest of the distribution. There is also a peak at  $90^\circ$  with a width of about  $10^\circ$  and a rather broad peak which extends from  $100^\circ$  to  $120^\circ$  and centers at about  $110^\circ$ . The corresponding angular distribution in the laboratory system is given in Fig. 3(b). Here, apart from the prominent peaks in the forward and backward directions (which are, respectively, two and one orders of magnitude higher than the rest), there is a rather broad peak which extends from  $66^\circ$  to  $100^\circ$  and peaks at  $85^\circ$ . The underlying components of this distribution can be further analyzed in greater detail from the energy distributions  $d^2N/dEd\Omega$ .

The forward peak comes from very slow particles of less than 5 MeV. They arise as a consequence of the stopping of the small projectile nucleus by a much larger target. The backward peak in the laboratory system consists mainly of low-energy particles of below 10 MeV and also some slightly more energetic particles of about 15 MeV. This arises from the expansion of the shock region to the backward direction. As the

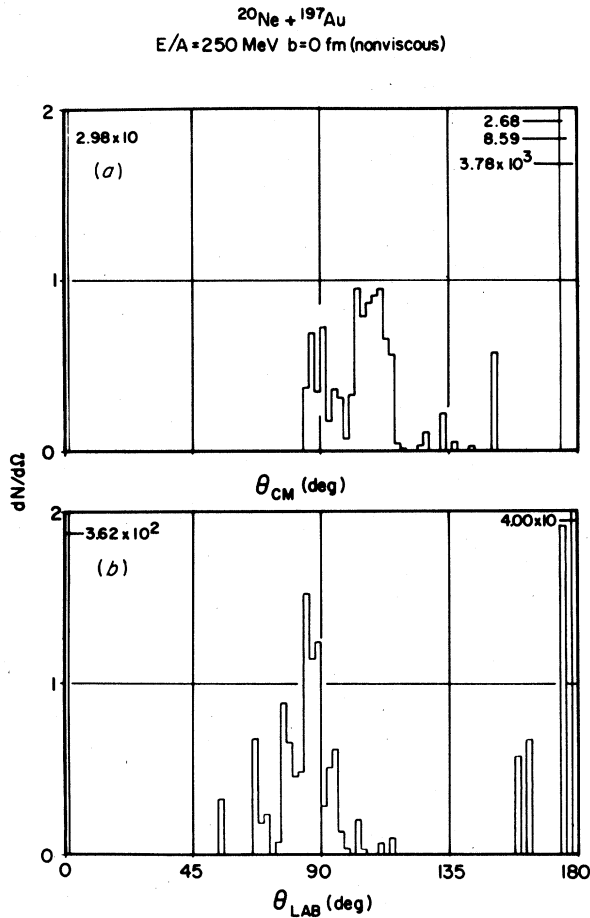


FIG. 3. (a) Angular distribution in the center-of-mass system for  $^{20}\text{Ne} + ^{197}\text{Au}$  at 250 MeV per nucleon with small viscosity. This and all other angular distributions hereafter are given in the same, but arbitrary, unit. To convert a given angular distribution into the absolute unit, that is, nucleon number/sr, multiply it by the factor of  $180/\pi$ . (b) Angular distribution in the laboratory system for  $^{20}\text{Ne} + ^{197}\text{Au}$  at 250 MeV per nucleon for the set of small transport coefficients given by Eq. (5.1).

expansion of the shock region at the early stage ( $\sim 25$  fm/c) is unhindered in this direction in contrast to the forward direction, slightly more energetic particles of about 15 MeV up to 30 MeV are also found in the backward direction, whereas the forward peak is restricted to particles below 5 MeV. The spectrum of particles in the side peak between  $60^\circ$  and  $100^\circ$  falls into roughly two groups. There is a large group of particles which peaks at about 19 and 31 MeV and a much smaller group of particles which peaks at about 65 MeV. The mean energy and standard deviation for different angular ranges are given in Table I(a).

To study the effects of the viscosity and thermal

conductivity on the dynamics, the calculation for  $^{20}\text{Ne}$  on  $^{197}\text{Au}$  at 250 MeV per nucleon is repeated with the larger values of the transport coefficients given in Eq. (5.2). The time evolution of the density field for this calculation is depicted in Fig. 4. In this case, though some features appear to be similar to the small viscosity case, there are, in fact, several distinct differences. First, in the small viscosity case, the thermal energy remains negligible (about 1 MeV at the most) throughout the entire reaction. In contrast, the larger viscosity and thermal conductivity lead to the generation of considerable thermal energy during the compression stage, with a maximum value of about 1400 MeV. The second difference lies in the density field. With large viscosity, the density profile is smoother and the maximum density reached ( $0.23 \text{ fm}^{-3}$ ) is smaller. That this is a viscosity effect can be understood as a consequence of the Navier-Stokes equations. There, the compressional viscosity gives a diffusion term associated with the current density field. Therefore, the greater the compressional viscosity, the greater is the rate of diffusion of the current density field. It is clear that when the compressional viscosity is large, any effect of density accumulation in a region, due to the influx of nuclear matter from the outside, will be reduced due to a competing diffusion process.

With small viscosity, the central density begins to drop below  $0.075 \text{ fm}^{-3}$  at about  $81.79 \text{ fm/c}$ , while with large viscosity, it begins to drop below this value at about  $96.87 \text{ fm/c}$ . These are the times at which the angular and energy distributions are extrapolated from the corresponding calculations. Detailed comparisons of these distributions for the nonviscous and viscous cases provide some interesting insight. For the large viscosity case, the angular distribution in the center-of-mass system is given in Fig. 5(a). This distribution has pronounced and narrow peaks in the forward and backward directions with a width of about  $2^\circ$ . There is also a peak at  $90^\circ$  with a width of about  $15^\circ$ . This is a simpler structure than the corresponding distribution in the small viscosity case (Fig. 3) for which there is a broad spectrum between  $90^\circ$  and  $135^\circ$ . The laboratory distribution  $dN/d\Omega$ , given in Fig. 5(b), has peaks at the forward and backward directions, and also a broad distribution between  $50^\circ$  and  $90^\circ$  with a peak at about  $67^\circ$ . In fact, except for the positions of the various peaks which are shifted by about  $18^\circ$ , this is very similar in shape to the corresponding distribution between  $60^\circ$  and  $100^\circ$  of the "small" viscosity calculation. (Compare Figs. 3 and 5.) Accordingly, the effect of viscosity in this case appears to give an over-

TABLE I. The angular distribution, mean energy, and energy width for collision of  $^{20}\text{Ne} + ^{197}\text{Au}$  at an energy of 250 MeV per nucleon. Table I(a) is for the case  $\eta = \zeta = 10^{-4} \text{ MeV}/(\text{fm}^2 c)$  and  $\kappa = 10^{-4} c/\text{fm}^2$  and Table I(b) for  $\eta = 0.75 \text{ MeV}/(\text{fm}^2 c)$ ,  $\zeta = 18.76 \text{ MeV}/(\text{fm}^2 c)$ , and  $\kappa = 0.014 c/\text{fm}^2$ . The quantity  $\bar{E}$  is the average energy within the angular bin and  $\sigma_E$  is the root-mean-squared energy within the bin.

$\theta_{lab}$ (deg)	(a)			(b)		
	$dN/d\Omega$	$\bar{E}$ (MeV)	$\sigma_E$ (MeV)	$dN/d\Omega$	$\bar{E}$ (MeV)	$\sigma_E$ (MeV)
0-20	181.0	1.16	0.55	206.6	1.13	0.50
20-40	0			0.184	3.18	1.06
40-60	0.16	7.00	0.50	0.908	6.30	2.68
60-80	1.35	21.2	11.6	4.19	27.0	13.5
80-100	3.52	23.7	16.4	0.60	38.3	16.4
100-120	0.22	16.3	13.7	0.04	24.7	13.3
120-140	0			0.002	9.0	0.50
140-160	0.29	1.00	0.50	0		
160-180	21.6	1.63	3.11	3.38	1.0	0.5

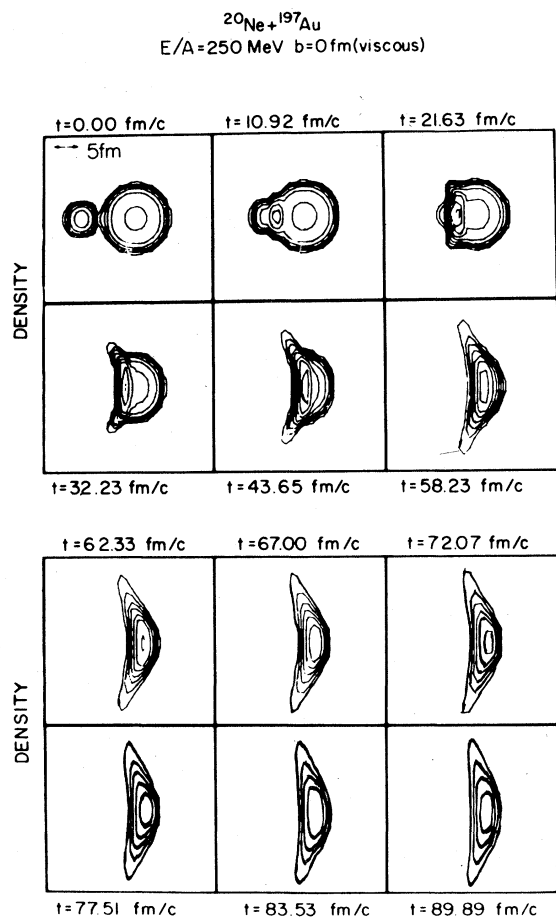


FIG. 4. Time evolution of the density field for  $^{20}\text{Ne} + ^{197}\text{Au}$  at 250 MeV per nucleon with large transport coefficients given by Eq. (5.2).

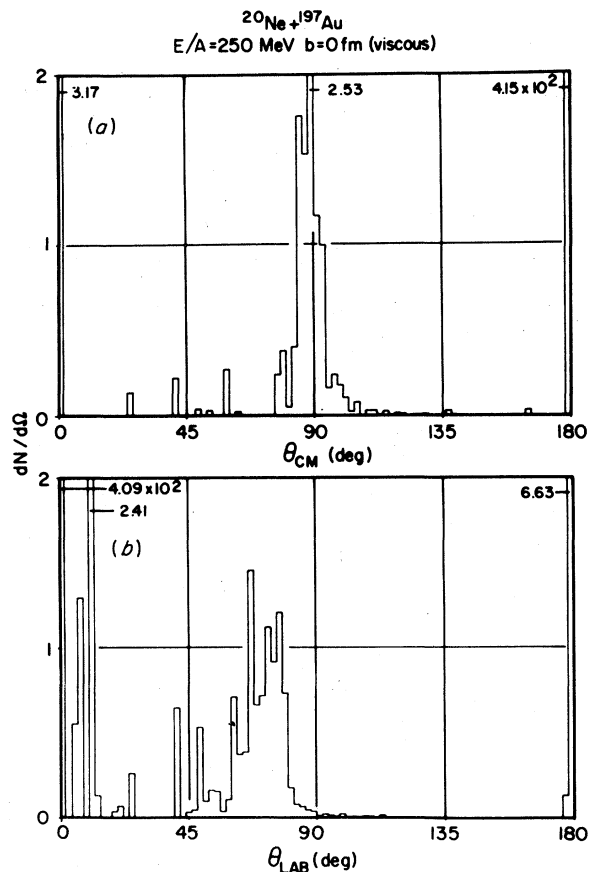


FIG. 5. (a) Angular distribution in the center-of-mass system for  $^{20}\text{Ne} + ^{197}\text{Au}$  at 250 MeV per nucleon with large viscosity [Eq. (5.2)]. (b) Angular distribution in the laboratory system for  $^{20}\text{Ne} + ^{197}\text{Au}$  at 250 MeV per nucleon with large viscosity [Eq. (5.2)].

all shift of the side angle peak toward smaller angles. This effect of dissipation will be systematically examined at the other energies and will be discussed again below. The mean energy and standard deviation for different angular ranges are given in Table I(b). The energy distributions in the laboratory system for the forward and backward peaks come from slow particles of below 5 and 10 MeV, respectively. This is a broad spectrum which first peaks at about 15 MeV, but drops slowly after that in an approximately exponential manner and extends to about 70 MeV. In the peak at the angular range  $60^\circ$ – $80^\circ$ , the mean energy is 27 MeV with a standard deviation of 16 MeV. These quantities are greater than the corresponding quantities in the small viscosity case. The effect of viscosity is to shift the energy of the side peak to a higher energy and also to increase the energy width.

#### B. $^{208}\text{Pb} + ^{208}\text{Pb}$ at 100 MeV per nucleon

Figure 6 depicts the reaction of  $^{208}\text{Pb} + ^{208}\text{Pb}$  at 100 MeV per projectile nucleon and for the small values of viscosity and thermal conductivity. At 18.24 fm/c, a central region of compressed nuclear matter is formed ( $\sim 0.25 \text{ fm}^{-3}$ ). This is only the beginning of the compression stage. The rest of the projectile and target nuclei are essentially unperturbed. They continue to come toward each other and maintain a constant influx of nuclear matter into the central compressed region. The maximum density reached in this reaction is  $0.30 \text{ fm}^{-3}$ . Similar to the nonviscous case of  $^{20}\text{Ne} + ^{197}\text{Au}$  discussed earlier (Fig. 2), the density profile of the shock region also has very sharp edges. A detailed study of the intermediate steps between 18.24 fm/c and 81.58 fm/c shows that the diffuseness of the "edge" of this shock region actually undergoes oscillation. (A hint of such an oscillation can be found by comparing the level spacing of the contours from time steps 35.76 fm/c to 107.06 fm/c in Fig. 6.) This is due to the tendency of the central region to expand outward even during the compression stage. Beginning at about 36 fm/c, there is ejection of nuclear matter in the  $90^\circ$  direction and eventually the composite system becomes disclike before the final overall expansion. The angular distribution  $dN/d\Omega$  in the center-of-mass system is given in Fig. 7(a). It has peaks at the forward and backward directions and at  $90^\circ$ . The angular distribution in the laboratory system is given in Fig. 7(b). Its main structure has peaks at the forward direction at  $7^\circ$  and at  $39^\circ$ . The forward peak consists of a group of

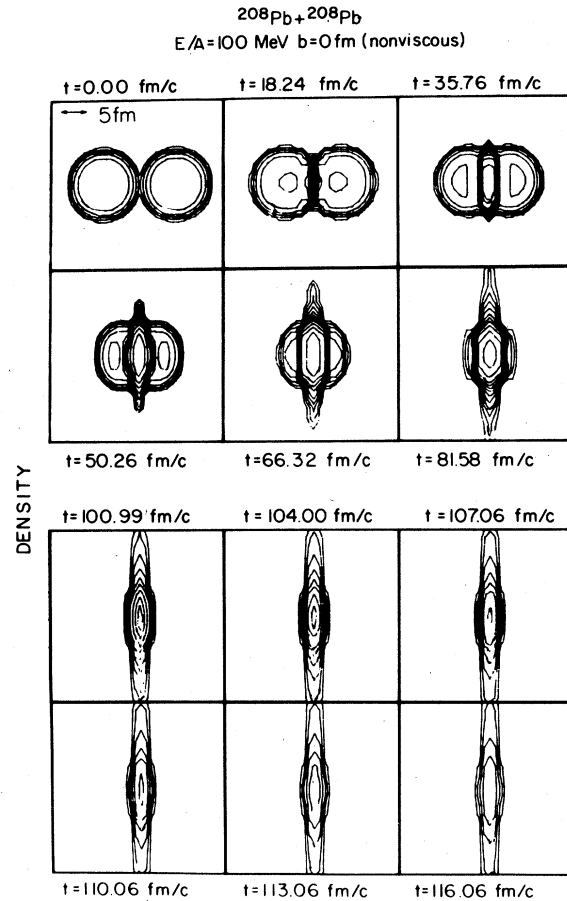


FIG. 6. Time evolution of the density field for  $^{208}\text{Pb} + ^{208}\text{Pb}$  at 100 MeV per nucleon with small viscosity [Eq. (5.1)].

particles of between 12 and 38 MeV, with a peak at about 23 MeV. The angular peak in the range between  $35^\circ$  and  $55^\circ$  consists of a broad spectrum of particles from 30 MeV up to 60 MeV, with a peak at about 39 MeV. The mean energy and standard deviation for different angular ranges are given in Table II(a). The mean energy and standard deviation increase as the angle increases until there is no cross section for  $\theta_{lab} \geq 60^\circ$ .

Figure 8 depicts the reaction  $^{208}\text{Pb} + ^{208}\text{Pb}$  at 100 MeV per nucleon with the set of large coefficients of viscosity and thermal conductivity [Eq. (5.2)]. The thermal energy generated during the compression stage ( $\sim 20$ – $70$  fm/c) reaches a maximum of about 1300 MeV. The maximum density attained in this reaction is  $0.23 \text{ fm}^{-3}$ . A comparison of the density plots with those of the small viscosity case (Fig. 7) reveals some differences. With large viscosity, the density profile remains very smooth during the entire compression stage. The maximum density is smaller than the small

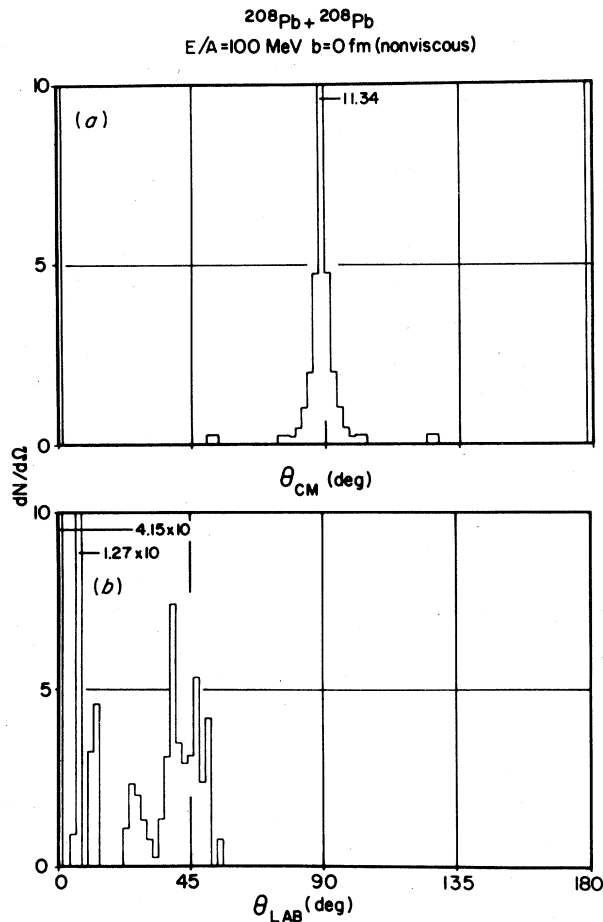


FIG. 7. (a) Angular distribution in the center-of-mass system for  $^{208}\text{Pb} + ^{208}\text{Pb}$  at 100 MeV per nucleon with small viscosity. (b) Angular distribution in the laboratory system for  $^{208}\text{Pb} + ^{208}\text{Pb}$  at 100 MeV per nucleon with small viscosity.

viscosity case. But once the maximum density is reached at about 36 fm/c, the system sustains this density for a longer period ( $\sim 36$ – $\sim 68$  fm/c). The

center-of-mass angular distribution is very similar to the small viscosity case, that is, sharp peaks at  $90^\circ$ ,  $0^\circ$ , and  $180^\circ$ . However, the laboratory angular distribution (Fig. 9) displays some small differences. The distribution between  $30^\circ$  and  $70^\circ$  has a shape which is roughly the same as that between  $20^\circ$  and  $60^\circ$  for the small viscosity case, with the exception that the position of the peaks are all shifted to a slightly larger angle. The mean energy and standard deviation for different angular ranges are given in Table II(b). The forward peak comes from a relatively narrow spectrum of particles which peaks at 23 MeV with a width of about 5 MeV. In the angular range between  $24^\circ$  and  $44^\circ$ , the particles have kinetic energies between 25 and 50 MeV, with the energy spectrum peaking at about 31 MeV. The energy distribution for the angular range between  $44^\circ$  and  $64^\circ$  is a broad spectrum extending from 30 MeV up to 100 MeV, peaking at about 55 MeV. There is also a small group of energetic particles of 90–100 MeV. This broad distribution is in contrast to the relatively narrower distribution for the small viscosity case for the angular range between  $35^\circ$  and  $55^\circ$ .

### C. Viscosity and energy dependence of angular distributions

In the detailed study of  $^{20}\text{Ne} + ^{197}\text{Au}$  at 250 MeV per nucleon and  $^{208}\text{Pb} + ^{208}\text{Pb}$  at 100 MeV per nucleon, we have seen how the angular distributions of the reaction products can be sensitive to the presence of dissipation. To firmly establish this dependence as a feature of the hydrodynamical description and also to study further the energy dependence of the angular distributions, we extend our calculations also to other energies.

Figures 10(a) and 10(b) show the angular distributions for the reaction  $^{20}\text{Ne} + ^{197}\text{Au}$  at 100 MeV

TABLE II. Same as Table I but for the case of  $^{20}\text{Ne} + ^{197}\text{Au}$  at an energy of 100 MeV per nucleon.

$\theta_{lab}$ (deg)	(a)			(b)		
	$dN/d\Omega$	$\bar{E}$ (MeV)	$\sigma_E$ (MeV)	$dN/d\Omega$	$\bar{E}$ (MeV)	$\sigma_E$ (MeV)
0–20	31.5	23.7	5.21	66.29	23.4	4.67
20–40	9.81	35.8	5.65	3.39	35.4	5.98
40–60	14.8	47.43	8.26	13.7	60.2	11.8
60–80	0			0.90	90.0	10.2
80–180	0			0		

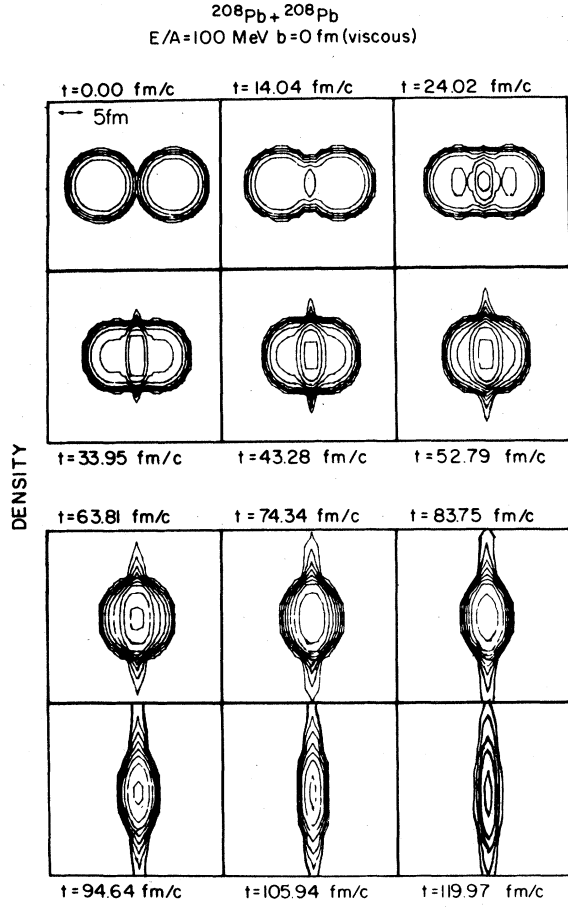


FIG. 8. Time evolution of the density field for  $^{208}\text{Pb} + ^{208}\text{Pb}$  at 100 MeV per nucleon with large viscosity.

per nucleon for small and large transport coefficients, respectively. In the small viscosity case [Fig. 10(a)], there are forward peaks, and the distribution between  $\sim 50^\circ$  and  $\sim 100^\circ$  is approxi-

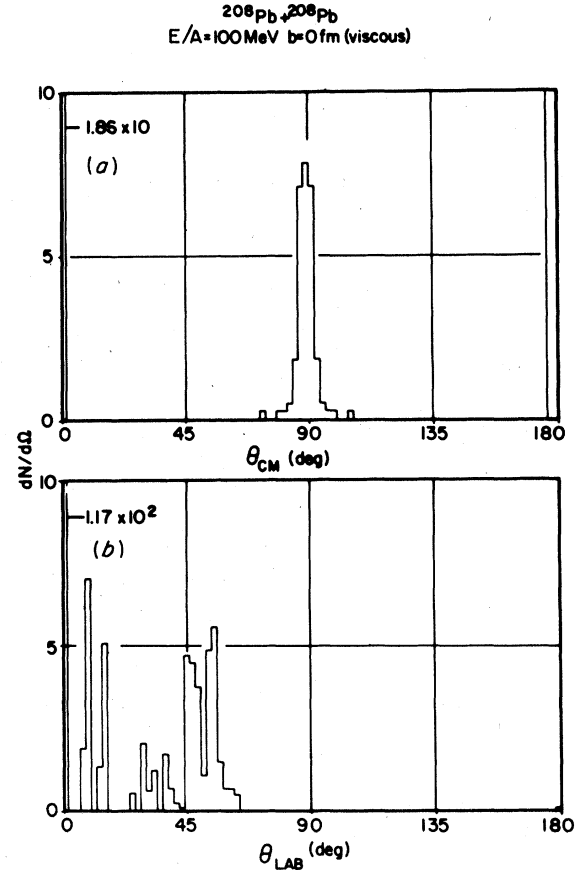


FIG. 9. (a) Angular distribution in the center-of-mass system for  $^{208}\text{Pb} + ^{208}\text{Pb}$  at 100 MeV per nucleon with large viscosity. (b) Angular distribution in the laboratory system for  $^{208}\text{Pb} + ^{208}\text{Pb}$  at 100 MeV per nucleon with large viscosity.

mately symmetrical and peaks at about  $73^\circ$ . In the large viscosity case [Fig. 10(b)], apart from forward and backward peaks, there is a broad

TABLE III. Same as Table I but for the case of  $^{20}\text{Ne} + ^{197}\text{Au}$  at an energy of 400 MeV per nucleon.

$\theta_{\text{lab}}$ (deg)	(a)			(b)		
	$dN/d\Omega$	$\bar{E}$ (MeV)	$\sigma_E$ (MeV)	$dN/d\Omega$	$\bar{E}$ (MeV)	$\sigma_E$ (MeV)
0-20	115.2	1.17	0.55	210	1.41	0.082
20-40	0			0.48	5.31	2.06
40-60	0			0.519	9.66	3.00
60-80	0.561	36.6	7.47	3.66	48.5	22.4
80-100	2.87	32.5	18.0	1.21	71.68	25.5
100-120	1.65	29.0	13.4	0.10	45.2	32.1
120-140	0.21	3.95	2.07	0		
140-160	0.28	1.0	0.5	0		
160-180	79.6	1.83	3.94	4.88	1.25	0.086

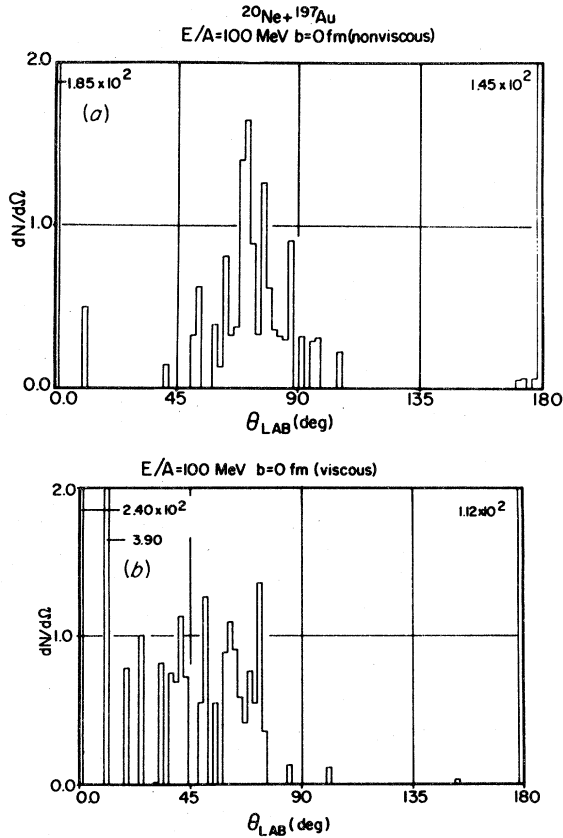


FIG. 10. (a) Angular distribution in the laboratory system for  $^{20}\text{Ne} + ^{197}\text{Au}$  at 100 MeV per nucleon with small viscosity. (b) Angular distribution in the laboratory system for  $^{20}\text{Ne} + ^{197}\text{Au}$  at 100 MeV per nucleon with large viscosity.

distribution extending from about  $10^\circ$  up to about  $75^\circ$ , and this distribution is distinctly different from that in the nonviscous case.

Figures 11(a) and 11(b) show the laboratory angular distributions of  $^{20}\text{Ne} + ^{197}\text{Au}$  at 400 MeV per nucleon for small and large viscosity, respectively. In both cases, apart from the forward and backward peaks, there is a peak at  $103^\circ$  for the small viscosity case and at  $73^\circ$  for the large viscosity case. With respect to the angular distribution, the effect of the presence of viscosity is to shift the side peak due to the backplash of nuclear matter from  $103^\circ$  to  $73^\circ$ . The mean energy and standard deviation for different angular ranges in the collision of  $^{20}\text{Ne} + ^{197}\text{Au}$  at 400 MeV per nucleon is given in Table III. One finds that the forward and backward peaks consist of nucleons with small kinetic energies. For the side peak, the mean energy is about 33 MeV and the standard deviation is 18 MeV for the small viscosity case. The mean energy

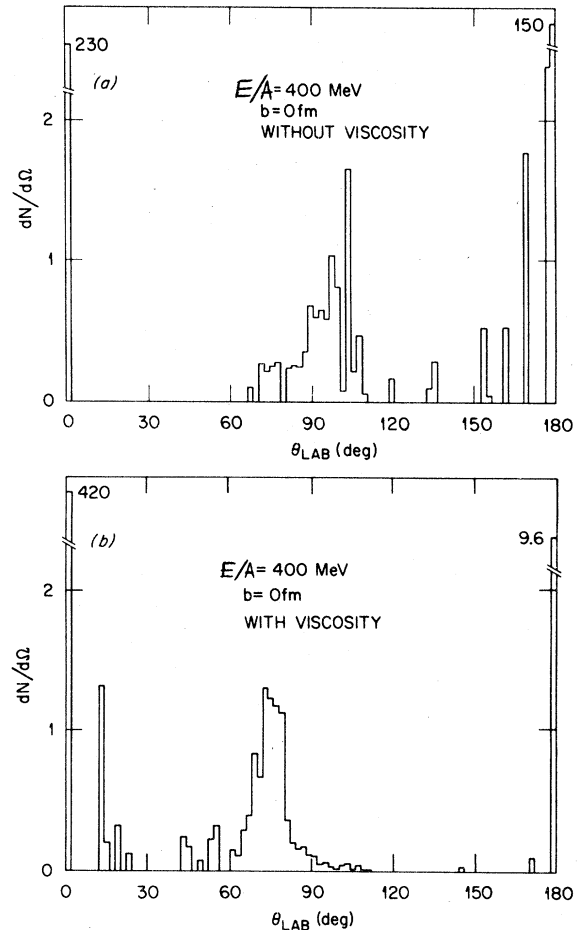


FIG. 11. (a) Angular distribution in the laboratory system for  $^{20}\text{Ne} + ^{197}\text{Au}$  at 400 MeV per nucleon with small viscosity. (b) Angular distribution in the laboratory system for  $^{20}\text{Ne} + ^{197}\text{Au}$  at 400 MeV per nucleon with large viscosity.

increases to 49 MeV and the standard deviation to 22 MeV for the large viscosity case. We hope to compare our results with the relevant high-multiplicity data of Gutbrod *et al.*<sup>7</sup> which is still being analyzed. Preliminary results<sup>7</sup> indicate the presence of sidesplash which is a feature of the hydrodynamical result.

Figures 12(a) and 12(b) are the angular distributions of  $^{208}\text{Pb} + ^{208}\text{Pb}$  at 50 MeV per nucleon for the nonviscous and viscous cases, respectively. Figures 13 and 14 are the angular distributions for the same reaction, but at 250 MeV per nucleon and Fig. 14, at 400 MeV per nucleon. There are some differences in the detailed shapes and heights of the peaks and small shifts in these distributions due to viscosity. The energy distributions also show some differences for the two cases, and the presence of viscosity tends to

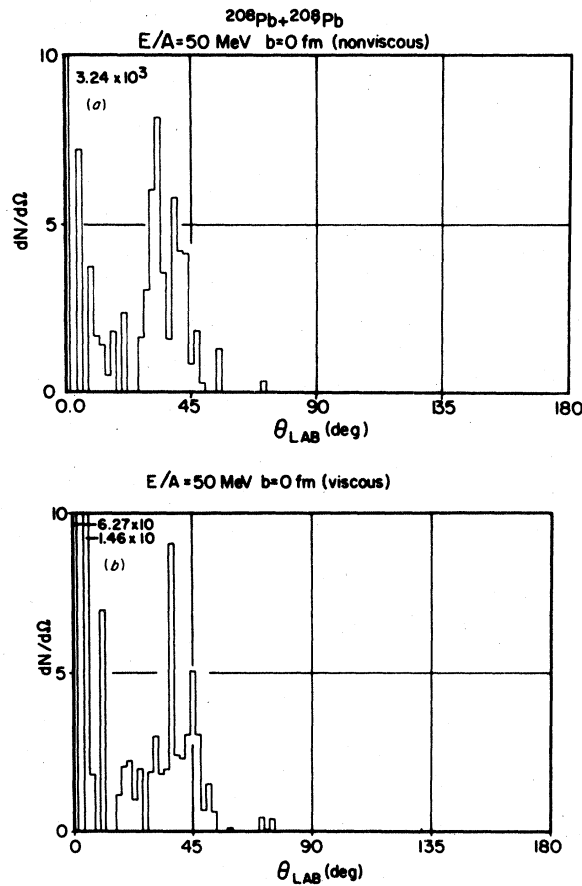


FIG. 12. (a) Angular distribution in the laboratory system for  $^{208}\text{Pb} + ^{208}\text{Pb}$  at 50 MeV per nucleon with small viscosity. (b) Angular distribution in the laboratory system for  $^{208}\text{Pb} + ^{208}\text{Pb}$  at 50 MeV per nucleon with large viscosity.

broaden the spectra. From the comparison of these results, one observes that the angular and energy distributions of the reaction products are sensitive to the presence of viscosity.

#### D. Compression ratio

Since the formation of compressed nuclear matter and its consequences are among the most important motivations for high-energy, heavy-ion physics, we shall study some of our results with these questions in mind. The main results of various calculations are compactly presented in Fig. 15. The curves are the compression ratios (maximum density/normal density) achieved in the  $^{20}\text{Ne} + ^{197}\text{Au}$  and  $^{208}\text{Pb} + ^{208}\text{Pb}$  reactions, plotted against bombarding energy. Each curve corresponds to one set of transport coefficients. It is clear from the figures that the compression ratio increases monotonically with increasing energy. Also, it appears that a

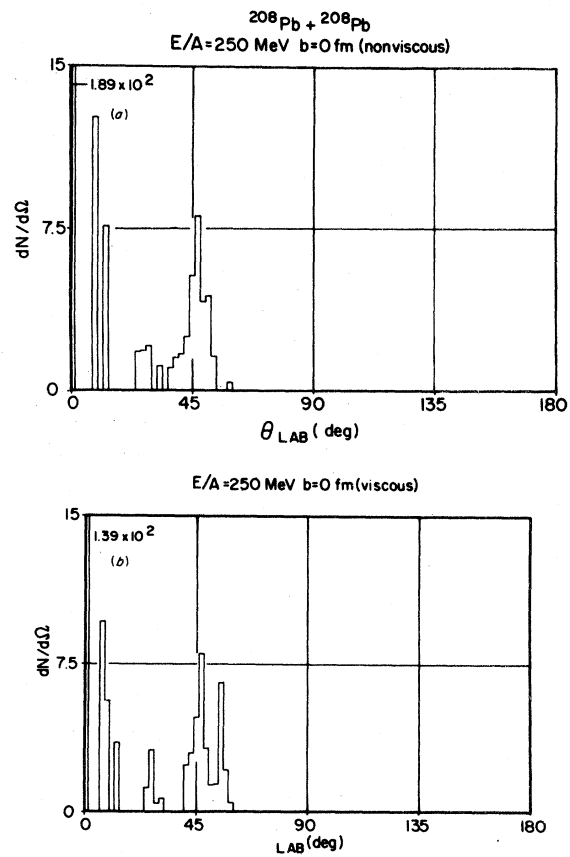


FIG. 13. (a) Angular distribution in the laboratory system for  $^{208}\text{Pb} + ^{208}\text{Pb}$  at 250 MeV per nucleon with small viscosity. (b) Angular distribution in the laboratory system for  $^{208}\text{Pb} + ^{208}\text{Pb}$  at 250 MeV per nucleon with large viscosity.

high compression ratio is favored more by large projectile-target systems.

The role played by the transport coefficient is rather significant. Large viscosity and thermal conductivity results in the generation of considerable thermal energy. Not only is the density profile smoothed out by a large viscosity, but the maximum density reached is also substantially reduced.

#### E. Other features

Though we are mainly concerned with high-energy reactions in this paper, it is noteworthy to remark that there are also many other special features of nuclear hydrodynamics which manifest themselves, particularly at lower energies.<sup>16</sup> A notable example is that for an expanding composite system, there is a tendency in the density field to form clusters when the colliding energy

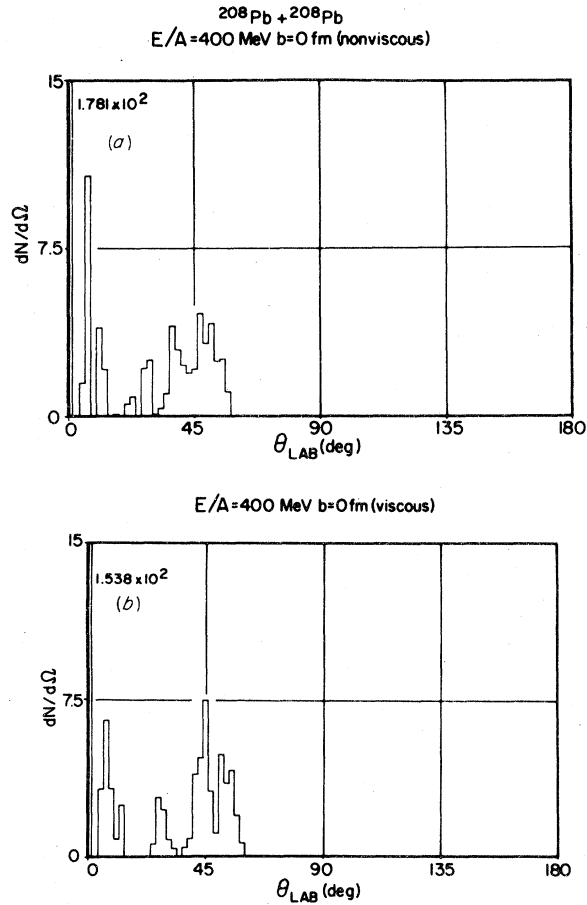


FIG. 14. (a) Angular distribution in the laboratory system for  $^{208}\text{Pb} + ^{208}\text{Pb}$  at 400 MeV per nucleon with small viscosity. (b) Angular distribution in the laboratory system for  $^{208}\text{Pb} + ^{208}\text{Pb}$  at 400 MeV per nucleon with large viscosity.

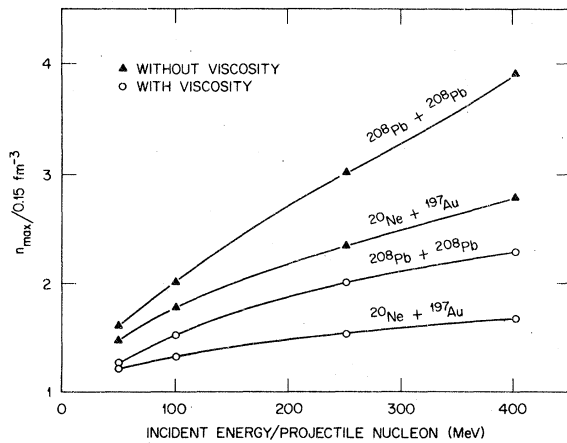


FIG. 15. Compression ratio attained in the collision of  $^{20}\text{Ne} + ^{197}\text{Au}$  and  $^{208}\text{Pb} + ^{208}\text{Pb}$ , with and without viscosity, as a function of bombarding energy.

is less than a certain limit. Above this energy, the nuclear matter is so much compressed in the shock region that when it expands, it keeps on expanding without collapsing back into clusters with normal nuclear matter density. This kind of behavior can be understood in terms of the shape of the equation of state  $E(n)$ . For small deviations of the density from equilibrium value,  $E(n)$  is approximately a parabola. However, for large values of deviation, it is a high wall for large densities but an open and relatively flat region for low densities. A highly compressed nuclear matter, after relaxing to the equilibrium density and going to the low density region, will have too high a kinetic energy in the density degree of freedom to come to a turning point.

Systematic studies of two-dimensional model collisions of columns of nuclear matter indicate that asymmetric collisions at an energy of  $E \geq 60$  MeV per nucleon lead to a complete dissociation of the composite system, while collisions at  $E \geq 40$  MeV per nucleon lead to self-bound clusters. In the three-dimensional head-on collisions, a clustering in the direction of the collision axis corresponds to a fissionlike behavior, while a clustering perpendicular to the collision axis corresponds to the formation of a ring of nuclear matter. In order to investigate this aspect, we perform calculations for  $^{20}\text{Ne} + ^{197}\text{Au}$  at 50 MeV with zero impact parameter. Figure 16 depicts the results for the small viscosity case. At about 70 fm/c, the composite system relaxes in response to the compression of nuclear matter. At 114.13 fm/c, we begin to see some clustering effect in the radial direction. At 198.70 fm/c, this eventually leads to the formation of a vortex ring of nuclear matter, with density of about  $0.075 \text{ fm}^{-3}$ . The central cluster has

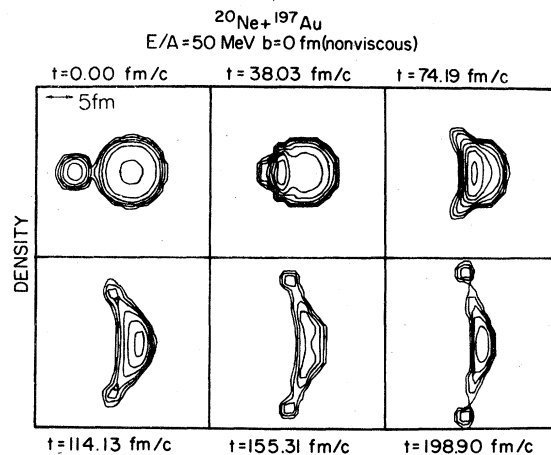


FIG. 16. Time evolution of the density field for  $^{20}\text{Ne} + ^{197}\text{Au}$  at 50 MeV per nucleon with small viscosity.

a normal density. At the end of the calculation, this ring goes toward to the right, while the central cluster goes in the opposite direction. The calculation is terminated here, since we do not know whether this configuration is a stable one. Nonaxial sausage-type instability is a very important mode.<sup>34</sup> Future calculations for very small but nonzero impact parameters will help to determine more firmly the detailed dynamics beyond this stage. The same calculation but with large viscosity shows that at the comparable time scale, the "clustering effect" and the ring formation are much less pronounced.

When we increase the energy of the projectile  $^{20}\text{Ne}$  to 100 MeV per nucleon, the density contour indicates that the density of the composite system keeps on decreasing after the shock region relaxes. There is no restriction of the nuclear matter density back to the equilibrium value, as was the case for the central cluster in the case of 50 MeV per nucleon (Fig. 16). One infers that 100 MeV per projectile nucleon is approximately the energy above which a head-on collision of the projectile  $^{20}\text{Ne}$  with  $^{197}\text{Au}$  will lead to a complete dissociation of the composite system. For the collision of  $^{208}\text{Pb}$  on  $^{208}\text{Pb}$ , one finds that a head-on collision with an energy above 50 MeV per nucleon will lead to a complete dissociation of the composite system.

#### F. Comparison with other results

Despite the difference of the emphasis in the present studies and the previous hydrodynamical calculations<sup>5-7</sup> which apply to the PIC method, it is still of interest to compare the two types of results whenever possible. Figure 3 of Ref. 8 presents the proton energy distribution for the reaction  $^{20}\text{Ne} + ^{238}\text{U}$  at 250 MeV per nucleon at zero impact parameter and for the laboratory angles  $30^\circ$ ,  $60^\circ$ ,  $90^\circ$ , and  $120^\circ$ . This can be compared with our calculation of  $^{20}\text{Ne} + ^{197}\text{Au}$  at the same bombarding energy and with small viscosity.

The general features of the energy distributions at  $60^\circ$ ,  $90^\circ$ , and  $120^\circ$ , predicted by the PIC method and the FCT method, agree well. In order to make some more quantitative comparisons, we reconstruct the four points in the angular distribution for the PIC energy distributions by a summation over the energy, taking into account that the proton spectrum is only  $\frac{102}{258}$  of the whole. We found that the two types of calculations using the PIC and FCT methods agree very well in the nonviscous case.

#### VI. SUMMARY AND CONCLUSION

Our systematic studies of  $^{20}\text{Ne} + ^{197}\text{Au}$  and  $^{208}\text{Pb} + ^{208}\text{Pb}$  at different energies have revealed several

interesting features of the hydrodynamical description. The angular distributions of the reaction products have prominent structures. Apart from sharp peaks in the forward and backward directions, there are distinct side peaks. The positions of the peak in this angular range tend to move toward larger angles with increasing bombarding energies. This is true in both the symmetric and asymmetric systems. The presence of dissipation also displays significant effects on the dynamics, in particular, on the maximum density in the intermediate steps of the reaction and also in the angular and energy distribution of the final reaction products. The viscosity dependence of the angular distribution is much more prominent in the asymmetric than the symmetric collisions. In the former case, the presence of viscosity can lead to a difference of as much as  $10^\circ$  to  $20^\circ$  in the positions of the angular peaks. The underlying energy distributions also show differences for the viscous and nonviscous cases. In general, they tend to be broadened by dissipation. Accordingly, future detailed comparisons with experimental distributions will provide a useful means to obtain the transport coefficients.

However, head-on collisions are rare events in heavy-ion reactions. In order to substantiate the present results, it is also necessary to extend the calculations to collisions with small, but nonzero impact parameters. Investigations of the three-dimensional calculations for near-head-on collisions which exploit axial symmetry, are now in progress (see Appendix) and the results will be available in the near future.

Even though head-on and near-head-on collisions are of special interest as a testing ground for nuclear hydrodynamics, these cases cannot be of much use if there were no way to select these events for scrutiny. Recently, a method for selecting these events was proposed<sup>35</sup> by one of us (C. Y. W.). This was based on the introduction of the concept of centrality as a measure of the deviation of the reaction products from the azimuthal symmetry. It is hoped that the method can be well developed and supplement the usual selection based on multiplicity, so that a direct confrontation of the present results with experiments can be made to provide the critical test on the validity of the hydrodynamical description for heavy-ion collisions.

Finally, it should be remarked that the studies reported here are done with a particular choice of the equation of state for the nuclear field. It is clear that to further our investigation, other functional forms can be attempted. It will be of great interest to compare various theoretical

predictions based on different forms of the equation of state. Final confrontations with experimental results will provide a unique probe into the details of this and also other properties of nuclear matter.

#### ACKNOWLEDGMENTS

The authors wish to thank Professor S. E. Koonin, Dr. M. R. Strayer, Dr. K. R. Sandhya Devi, Professor R. Y. Cusson, Dr. D. L. Book, Dr. D. K. Scott, Dr. H. H. Gutbrod, and the Theory Group at Oak Ridge for their helpful communications and suggestions during various states of this work. One of us (H.H.K.T.) wishes to thank Professor D. A. Bromley for his kind encouragement and valuable discussions, and Dr. P. H. Stelson and Dr. J. B. McGrorey for their kind hospitality at Oak Ridge National Laboratory where this work was carried out. This research was sponsored by the U. S. Department of Energy under Contract Nos. EY-76-C-023074 with Yale University and W-7405-eng-26 with the Union Carbide Corporation. H. H. K. Tang is grateful for the support of an F. W. Heyl and Elsie L. Heyl Predoctoral Fellowship. Much of the work reported here is based on part of a thesis submitted by H. H. K. Tang to Yale University in partial fulfillment of the requirements of the Ph.D. degree.

#### APPENDIX: NUMERICAL METHODS OF NUCLEAR HYDRODYNAMICS

The numerical algorithms to solve the hydrodynamical equations (2.1)–(2.3), are based on the flux-corrected-transport (FCT) method and the time-step-splitting (TSS) method of Boris and Book.<sup>18</sup>

These methods lead to a class of Eulerian finite-difference schemes which are found to be numerically stable and accurate. The FCT algorithm solves a one-dimensional generalized continuity equation (i.e., with source term) in the following manner. The propagation of a dynamical variable over a time step is achieved in two stages. In the convection stage the dynamical variable is followed in time in a Lagrangian manner. The transient profile of the variable is then extrapolated back onto the original Eulerian grid points in such a way that the conservation of total mass is enforced and the positivity of the mass density and energy density guaranteed. This, however, introduces inherent errors due to diffusion. These are corrected in the anti-diffusion stage which leads to the final solution.

The multidimensional problem is solved by means of the TSS method in the following way. Each time step is divided into two halves. A dynamical variable is propagated (by an operator from the FCT algorithm) in one direction through the first half step. The velocity along this direction is estimated. Then the variable is propagated through the entire time step using this velocity and the initial values at the beginning of the time cycle. This procedure is then repeated to the other directions.

Various details of the implementation of the FCT and TSS methods have been discussed previously<sup>18</sup> and will not be repeated here.

In computations which treat the three-dimensional geometry exactly, there are unavoidable problems of storage and speed. However, since we are mostly interested in head-on and near-head-on collisions in nuclear hydrodynamics, such computational problems may be circumvented. The results discussed here are obtained from a special 3D code which solves the problem as follows. In near-head-on collisions, the configuration of the density field is approximately symmetric. Hence, at each time step, we search for an approximate symmetry axis about which the density field is then axially symmetrized. All the dynamical variables are solved on the reaction plane. In this way, the three-dimensional problem is treated by a set of two-dimensional equations which include additional terms to take into account the other degree of freedom in an approximate way. In the limit of zero impact parameters, however, this method is exact for both collisions of symmetric and asymmetric systems.

As a consequence of these special considerations, this 3D code achieves a speed comparable to a 2D code but requires no additional storage. For a typical configuration of  $64 \times 64$  grid points, with a grid size of 0.6 to 1.2 fm and a time step interval of 0.6 to 1.5 fm/c, depending on the actual input, output, and other special implementations, this 3D code requires only 3 to 3.5 cpu second per time step on the 360/91 computer at Oak Ridge National Laboratory.

This can easily accommodate studies of heavy systems such as  $^{208}\text{Pb} + ^{208}\text{Pb}$ . For low energies ( $E/A \leq 50$  MeV), a typical reaction requires 400 to 600 time steps. For energies over 100 MeV/nucleon, however, it takes only about 100 to 200 time steps. Hence, from a practical point of view, such hydrodynamical calculations are well within the realm of possibilities of present computing facilities.

- \*Present address: Center for Theoretical Physics, Massachusetts Institute of Technology, Cambridge, Mass. 02139.
- <sup>1</sup>See, e.g., review article by A. S. Goldhaber and H. H. Heckman, *Annu. Rev. Nucl. Sci.* **28**, 161 (1978).
- <sup>2</sup>G. F. Bertsch, *Nucl. Phys.* **A249**, 253 (1978).
- <sup>3</sup>C. Y. Wong, J. A. Maruhn, and T. A. Welton, *Nucl. Phys.* **A253**, 469 (1975).
- <sup>4</sup>C. Y. Wong and J. A. McDonald, *Phys. Rev. C* **16**, 1196 (1977).
- <sup>5</sup>A. A. Amsden, F. H. Harlow, and J. R. Nix, *Phys. Rev. C* **15**, 2059 (1977).
- <sup>6</sup>A. A. Amsden, A. G. Goldhaber, F. H. Harlow, and J. R. Nix, *Phys. Rev. C* **17**, 2080 (1978).
- <sup>7</sup>H. H. Gutbrod, in *Proceedings of the Fourth High Energy Heavy-Ion Summer Study*, Berkeley, 1978, Report No. LBL-7766.
- <sup>8</sup>A. A. Amsden, J. N. Ginocchio, F. H. Harlow, J. R. Nix, M. Danos, E. C. Halbert, and R. K. Smith, Jr., *Phys. Rev. Lett.* **38**, 1055 (1977).
- <sup>9</sup>G. D. Westfall, J. Gosset, P. J. Johansen, A. M. Poskanzer, W. G. Meyer, H. H. Gutbrod, A. Sandoval, and R. Stock, *Phys. Rev. Lett.* **37**, 1202 (1976).
- <sup>10</sup>A. A. Amsden, G. F. Bertsch, F. H. Harlow, and J. R. Nix, *Phys. Rev. Lett.* **35**, 905 (1975).
- <sup>11</sup>W. Scheid, H. Müller, and W. Greiner, *Phys. Rev. Lett.* **32**, 741 (1974).
- <sup>12</sup>H. G. Baumgardt, J. U. Schott, Y. Sakamoto, E. Schopper, H. Stöcker, J. Hofmann, W. Scheid, and W. Greiner, *Z. Phys.* **A273**, 359 (1975).
- <sup>13</sup>C. Y. Wong and T. A. Welton, *Phys. Lett.* **49B**, 2431 (1974).
- <sup>14</sup>C. Y. Wong, J. A. Maruhn, and T. A. Welton, *Phys. Lett.* **66B**, 19 (1977).
- <sup>15</sup>H. H. K. Tang and C. Y. Wong, ORNL Physics Division Annual Progress Report No. ORNL-5306, 1977, pp. 138-142; *Bull. Am. Phys. Soc.* **22**, 645 (1977); C. Y. Wong and H. H. K. Tang, *ibid.* **23**, 586 (1978).
- <sup>16</sup>H. H. K. Tang, Ph.D. thesis, Yale University, 1979 (unpublished).
- <sup>17</sup>J. A. Maruhn, in *Proceedings Topical Conference on Heavy-Ion Collisions*, Fall Creek Falls State Park, Pikeville, Tenn., June 1977, Report No. CONF-770602.
- <sup>18</sup>J. P. Boris and D. L. Book, *J. Comput. Phys.* **11**, 38 (1973); D. L. Book, J. P. Boris, and K. Hain, *ibid.* **18**, 248 (1975); J. P. Boris and D. L. Book, *ibid.* **20**, 397 (1976).
- <sup>19</sup>M. I. Sobel, P. J. Siemens, J. P. Bondorf, and H. A. Bethe, *Nucl. Phys.* **A251**, 502 (1975).
- <sup>20</sup>C. Y. Wong and H. H. K. Tang, *Phys. Rev. Lett.* **40**, 1070 (1978); *Phys. Rev. C* **20**, 1419 (1979).
- <sup>21</sup>C. Y. Wong, ORNL report (unpublished).
- <sup>22</sup>K. Huang, *Statistical Mechanics* (Wiley, New York, 1963), Chap. 6.
- <sup>23</sup>C. Y. Wong and C. Toepffer in *Proceedings of Topical Conference on Large Amplitude Collective Nuclear Motions*, Keszthely, Hungary, June, 1979, p. 400.
- <sup>24</sup>J. Randrup, *Nucl. Phys.* **A314**, 429 (1979).
- <sup>25</sup>G. Bertsch, *Z. Phys.* **A289**, 103 (1978).
- <sup>26</sup>B. Tamain, R. Cechik, H. Fuchs, F. Hanappe, M. Morjean, C. Ngô, J. Peter, M. Dakowski, B. Lucas, C. Mazur, M. Ribrag, and C. Signarbieux, Orsay report, 1979.
- <sup>27</sup>G. Baym and C. Pethick, in *Physics of Liquid and Solid Helium*, Part II, edited by K. H. Bennemann and J. B. Ketterson (Wiley, New York, 1978).
- <sup>28</sup>J. Sykes and G. A. Brooker, *Ann. Phys. (N.Y.)* **56**, 1 (1970).
- <sup>29</sup>M. A. Preston, *Physics of the Nucleus* (Addison-Wesley, Reading, Mass., 1962), p. 93.
- <sup>30</sup>S. Nagamiya, in *Proceedings of Fourth High Energy Heavy-Ion Summer Study*, Berkeley, 1978, Report No. LBL-7766, Fig. 2.17.
- <sup>31</sup>M. N. Harekeh *et al.*, *Phys. Rev. Lett.* **38**, 676 (1977).
- <sup>32</sup>K. A. Brueckner, J. R. Buchler, R. C. Clark, and R. J. Lombard, *Phys. Rev.* **187**, 1543 (1969); H. A. Bethe, *Annu. Rev. Nucl. Sci.* **21**, 93 (1971).
- <sup>33</sup>C. Y. Wong, *Phys. Rev. C* **17**, 1832 (1978).
- <sup>34</sup>C. Y. Wong, *Ann. Phys. (N.Y.)* **77**, 279 (1973).
- <sup>35</sup>C. Y. Wong, *Phys. Lett.* **88B**, 39 (1979).